Influence of fracture intersections under unsaturated, low-flow conditions

Thomas R. Wood
Idaho National Engineering and Environmental Laboratory, Idaho Falls, Idaho, USA

Michael J. Nicholl
Geoscience Department, University of Nevada, Las Vegas, Nevada, USA

Robert J. Glass
Flow Visualization and Processes Laboratory, Sandia National Laboratories, Albuquerque, New Mexico, USA

Received 16 April 2004; revised 4 August 2004; accepted 4 February 2005; published 27 April 2005.

[1] Recent experimental evidence suggests that the capillary heterogeneity associated with fracture intersections can act to impose temporal and spatial structure on network-scale flows. A simple intersection between orthogonal fractures, one horizontal and the other vertical, has been shown to integrate unsaturated flows. At low flows the intersection forms a capillary barrier that accumulates water in a growing pool. Eventually, the retaining meniscus snaps, discharging a pulse of water. Here we develop a mechanistic explanation for this observed behavior and experimentally consider three perturbations to the geometry of the simple orthogonal intersection. Two of the perturbations also act as capillary barriers, while the third formed a capillary bridge across the intersection. At low flow, all of our experimental intersections imposed a temporal signal, with the nature of that signal dependent on intersection geometry and participation by the horizontal fractures in dynamic storage. At high flow a continuous fluid tendril spanned the system from inlet to outlet with water pooled above the intersection caused by a narrow fluid connection that restricted flow across the intersection. Results from all experiments suggest that pulsation is critically sensitive to small variations in the geometry of fracture intersections and storage in the horizontal fractures. When combined with dependency on supply rate, this sensitivity can generate pulsation of flow across a wide range of time periods and discharge volumes.

Citation: Wood, T. R., M. J. Nicholl, and R. J. Glass (2005), Influence of fracture intersections under unsaturated, low-flow conditions, *Water Resour. Res.*, *41*, W04017, doi:10.1029/2004WR003281.

1. Introduction

[2] Field evidence from arid environments often indicates that percolation of water through fractured rock vadose zones is spatially focused, rapid, and deep [e.g., *Russell et al.*, 1987; *Fabryka-Martin et al.*, 1996; *Yang et al.*, 1996; *Davidson et al.*, 1998]. Although the evidence for the occurrence of such flows is compelling, data from unforced natural systems is an end product that provides limited information regarding the contributing processes. Small-scale field experiments [e.g., *Nativ et al.*, 1995; *Dahan et al.*, 1999; *Faybishenko et al.*, 1998, 2000; *Podgorney et al.*, 2000; *Glass et al.*, 2002a; *Nicholl and Glass*, 2002] aid in the identification of those processes, but do not always lead to unambiguous interpretations. It is also difficult to control, monitor, or characterize such tests, let alone to systematically vary critical parameters. Thus, in order to properly understand natural flows, field observations must be interpreted in light of basic physical laws, and the interplay between those laws must be explored under controlled laboratory conditions.

0043-1397/05/2004WR003281$09.00

[3] Considering basic fluid mechanics, the deep penetration of water should be expected in arid fractured rock environments. Water is much denser than air, and will thus form gravity-driven fingers when applied to the top of an air-filled (dry) fracture. Gravity-driven fingers have been studied experimentally in both natural and analog fractures [*Nicholl et al.*, 1992, 1993a, 1993b, 1994; *Glass and Nicholl*, 1996; *Su et al.*, 1999] and demonstrated to occur in fractures adjacent to an absorbent matrix [*Glass and Tidwell*, 1991]. Gravity-driven fingers may also occur in unstable film flows along the surfaces of matrix blocks [e.g., *Glass et al.*, 2002b]. However, fractured rock is not composed simply of individual fractures. At the network scale the importance and influence of the capillary heterogeneity imposed by fracture intersections is not fully understood. A remaining, unresolved question is whether the effects of gravity-driven fingering will be mitigated through contact with multiple fracture intersections, or perhaps be modified to create an entirely new behavior.

[4] Experimental evidence gathered from many laboratory experiments conducted in single fractures and single fracture-matrix systems led *Glass et al.* [1995, 1996] to hypothesize that fracture intersections would act as capil-

lary barriers and focus flow with depth to impose spatial structure at the network scale. Recently, *LaViolette et al.* [2003] tested this hypothesis experimentally in a small two-dimensional porous matrix dissected by a regular fracture network. They found that at the scale of the experiment, intersections acted to focus flow in some realizations, but not in others. Thus fracture intersections may both split and focus flow. Such dual behavior has also been suggested by a simple field experiment where a dyed fluid slug was infiltrated from a surface pond [*Glass et al.*, 2002a; *Nicholl and Glass*, 2002]. Excavation and mapping of dyed fractures showed a structurally complex flow field where pervasive flow near the pond fragmented with depth to form multiple pathways. Fragmentation presumably occurred as a result of the transition from saturated (positive pressure) to unsaturated (tension) conditions. *Glass et al.* [2003] later found that certain intersection geometries and orientations can act to inhibit lateral spreading, and thus maintain slender pathways through fracture networks.

[5] In addition to the creation of spatial structure, fracture intersections have also been shown to impose a temporal signal on unsaturated flows. An experiment performed in an $\sim$2 m tall analog fracture-matrix network demonstrated temporal fluctuations within the network over a wide range of timescales [*Glass et al.*, 2002b]. Flow was found to pulse along individual pathways, and to also switch between pathways in time. Temporal fluctuations in outflow were larger than could be explained by simple pulsation along gravity-driven fingers within individual fractures [e.g., *Nicholl et al.*, 1993a; *Su et al.*, 1999]. As an alternate mechanism, they suggested that fracture intersections could act as hysteretic gates and switches. In this conceptualization, fracture intersections create capillary barriers that accumulate flow from above in a ''pool'', and then discharge a portion of the pool volume when the barrier is breached, thus turning steady inflow into pulsed outflow. This integrative behavior was confirmed by *Wood et al.* [2002] in experiments that considered flow across a simple intersection between two constant aperture fractures, one vertical and the other horizontal. At low flows their intersection accumulated fluid, and then discharged the integrated volume at periodic intervals. The intersection did not impose a temporal signal at somewhat higher flow rates. Behavior of a similar nature was observed in a transparent analog fracture network [*Glass et al.*, 2003]. *Dragila and Weisbrod* [2004] observed complex dynamics in the form of mode switching between aperture-spanning and film flow at an intersection where a vertical fracture split into two perpendicular fractures dipping at 45°. Most recently, *Ji et al.* [2004] observed that the ability of a fracture intersection to impose a temporal signal was highly dependent on the wetting properties of the flowing fluid.

[6] Behavior at fracture intersections will be controlled by competition between capillary, gravitational, viscous, and inertial forces. The balance between these forces will be highly dependent on intersection geometry. While little is known regarding the physical nature of fracture intersections in natural rock units, we expect intersection geometry to vary with mechanical properties and stress history of the rock unit. Geometric variables that will influence unsaturated flow include: the number of fractures intersecting, continuity of individual fractures (i.e., dead ends), fracture offsets, topology of the individual fractures, angle of intersection, and localized shattering or microfractures. In addition to simple geometric considerations, we expect behavior at intersections to be influenced by: the fluid phases involved (air, water, NAPL), surface chemistry, capillary hysteresis, initial fluid structure, secondary alteration (e.g., coatings, fillings, weathering rinds), biologic activity, interactions with the adjacent rock matrix, the nature of flow(s) entering the intersection (i.e., direction, velocity, timing), and finally, coupling between behavior at adjacent intersections.

[7] Here we focus on the action of a single fracture intersection to impose a temporal signal on unsaturated flows. We expand on the work of *Wood et al.* [2002] to explore behavior at a simple intersection between a horizontal fracture and a vertical fracture that forms an orthogonal cross. We also consider three perturbations to this simple geometry. Without changing topology of the fractures we consider vertical and horizontal offsets of the intersection, and a capillary bridge where detritus is lodged within the intersection to form a local connection. In section 2 we examine the mechanisms for formation and breaching of capillary barriers at these intersection geometries. Simple calculations show that fracture aperture will have a first-order influence on the balance between capillary, gravity, viscous, and inertial forces that controls system behavior. In section 3 we present an experimental design that allows us to observe intersection behavior as a function of the critical control parameter of supply rate. For construction of the experiments, fracture aperture was chosen to encourage competition between the controlling forces. Experimental observations of temporal response at each intersection geometry are presented in section 4. We discuss the commonalities and differences between the intersection geometries in section 5 and also infer their different influences at the network scale. Finally, we summarize our results in section 6.

2. Mechanistic Behavior at Idealized Intersections

[8] Given the range of possibilities for natural fractures, we focus here on a simplistic geometry that we believe to be ubiquitous in nature, the intersection between two mutually perpendicular fractures, one horizontal and the other vertical. We further assume that both fractures have a constant aperture, b (L), and that b is sufficiently small to support aperture-spanning menisci of the wetting phase (water). Where both fractures are throughgoing (Figure 1a), the intersection forms an orthogonal cross (OC). Naturally occurring perturbations to the OC geometry will include a small horizontal offset of the vertical fracture (Figure 1b), which we call a cross with horizontal offset (CHO), and a small vertical offset of the horizontal fracture (Figure 1c), which we call a cross with vertical offset (CVO). Each of these intersections forms a larger void space than the contributing fractures and is thus expected to act as capillary barriers to the wetting phase. We also consider a scenario where the intersection is locally spanned by solid material in the form of an asperity or detritus (Figure 1d), which we call a capillary bridge (CB). The bridge is expected to support a

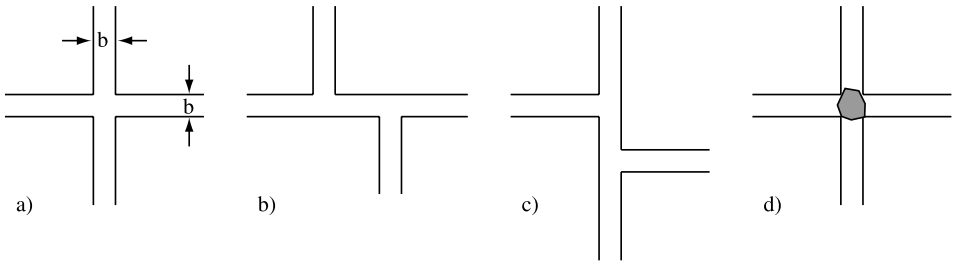

Figure 1. Our experimental investigation considered four fracture intersection geometries: (a) orthogonal cross (OC), (b) cross with horizontal offset (CHO), (c) cross with vertical offset (CVO), and (d) capillary bridge. All intersections are projected into the page, noting that the bridge in Figure 1d (gray blob) is a limestone pebble that establishes a point connection.

local (i.e., point) capillary connection across the intersection. Our definition of a capillary bridge involves a solid connection and thus differs from that of *Dragila and Weisbrod* [2004], who employed the term to describe an aperture spanning water droplet.

[9] In recent work considering the OC [*Wood et al.*, 2002] and CVO [*Glass et al.*, 2003] geometries, each has been observed to form a capillary barrier with the ability to act as a hysteretic gate to low flows. Gravity-driven fingers in the fracture above transport water to the intersection either continuously or in discrete pulses. When the gate is closed, the intersection integrates inflow into dynamic storage. Water is pooled in the vertical fracture above the barrier and possibly in the adjoining horizontal fracture(s). When the gate opens, discharge from dynamic storage through the intersection is at first rapid. As pool height falls, flow decreases and increased tension is applied by the downward growing fluid body, the gate closes and the capillary barrier is reestablished. When strong enough, viscous and inertial forces may prevent the gate from closing, and thus limit behavior as a capillary barrier. Under these conditions, flow through the constricted capillary connection across the intersection keeps the ''capillary constriction'' open against capillary forces, as has been argued by *Glass et al.* [2003].

[10] In this section we first (section 2.1) consider the mechanisms which lead to the formation and breaching of capillary barriers at the intersections shown in Figure 1. We also estimate the breaching pressure under quasi-static conditions by using interfacial geometry to weigh the balance between capillary and gravity forces. Breaching of a capillary barrier leads to discharge of the stored fluid volume and subsequent reestablishment of the capillary barrier; the controlling mechanisms are discussed in section 2.2. This section then concludes by considering the relative influence of viscous and inertial forces (section 2.3).

2.1. Formation and Breaching of Capillary Barriers

[11] The intersections shown in Figure 1 will form capillary barriers to the slow displacement of a nonwetting phase (air) by a wetting phase (water). In Figure 2 we have drawn idealized two-dimensional representations of the various meniscus configurations that occur at capillary barriers within the OC (Figures 2a and 2b), CHO (Figures 2c and 2d), and CVO (Figure 2e) intersections. In each, water arriving at an air-filled intersection will be blocked and spread laterally (into the page) to pool across the full width of the fracture. The configuration of trapped pools immediately after intersection discharge is shown in black and the configuration of pools and menisci immediately prior to discharge is shown in grey. The OC is shown with two configurations; Figure 2a represents a highly idealized situation where perfect geometry leads to symmetric behavior. Figure 2b represents the more likely configuration reported by *Wood et al.* [2002], where discharge involves at least partial filling of a horizontal fracture. Fluid pressure increases with pool height above the intersection, eventually causing the air-water meniscus to flatten and invade the intersection. The capillary barrier is breached when the meniscus crosses the intersection and contacts the opposite side as shown in gray (Figure 2).

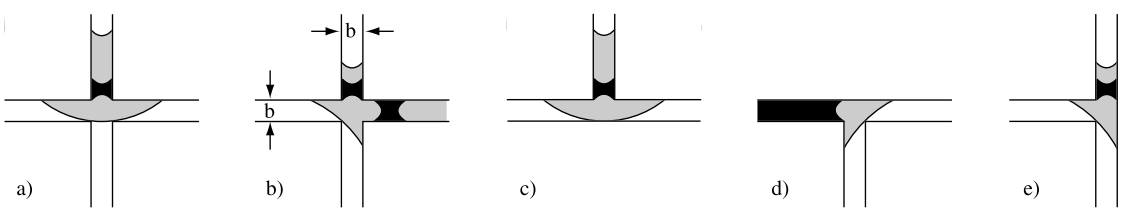

Figure 2. Cross-sectional views of potential capillary barriers at intersections between a horizontal and a vertical fracture. Wetting fluid initially pooled at the barrier is shown in black, while gray represents the fluid configuration when the barrier is breached: (a) OC (Figure 1a) breaching in symmetric fashion, (b) OC (Figure 1a) breaching first into one of the horizontal fractures, (c) inverted ''T'' intersection in the CHO (Figure 1b), (d) normal ''T'' intersection in the CHO (Figure 1b), and (e) sideways ''T'' intersections for the CVO (Figure 1c) will be reflections of one another.

[12] Under static conditions, pressure jump across the air-water interfaces shown in Figure 2 will be related to interfacial curvature by the Laplace-Young relation:

$$\psi = \frac{-\sigma}{\rho_w g}\left(\frac{1}{r_1}+\frac{1}{r_2}\right) \quad (1)$$

where ψ [L] represents fluid pressure per unit weight of water, σ is the air-water surface tension [M/T^2], ρ_w is the density of water [M/L^3], and g represents gravity [L/T^2]; r_1 and r_2 are the major and minor radii of curvature [L], respectively. If the fracture width, w [L], is $\gg$ the uniform fracture aperture, b [L], the top and bottom surfaces of the pool will be essentially flat in the plane of the fracture ($r_2 \rightarrow \infty$), and r_1 will equal $b/2$ modified by the air-water-solid contact angle (α). Note that α will likely differ between advancing and receding conditions. The pressure jump across the meniscus at the top of the pool (ψ_{top}) is inherently negative with respect to atmospheric pressure, and is given by

$$\psi_{top} = \frac{-2\sigma\cos\alpha}{\rho_w g b} \quad (2)$$

Height of fluid within the pool (h_p) acts against capillarity, and reduces the pressure jump across the meniscus at the bottom of the pool (ψ_{bottom}), such that

$$\psi_{bottom} = \psi_{top} + h_p \quad (3)$$

Since (1) will also hold for interfacial curvature along the bottom meniscus, the principal radius of curvature will increase with h_p, reaching infinity (i.e., bottom of the pool is flat) when $h_p = -\psi_{top}$ ($\psi_{bottom} = 0$). Note that $-\psi_{top}$ also gives the capillary rise.

[13] By assuming a nonzero contact angle, we can use geometric considerations to predict the pool height ($h_{\max}$) required to breach the intersection as shown in Figure 2a:

$$h_{\max} = \frac{\sigma}{\rho_w g b}\left[2\cos\alpha + \frac{\sin^2\alpha}{\cos\alpha - \sqrt{1+\frac{\sin^2\alpha}{4}}}\right] \quad (4)$$

Addition of water to a pool causes it to grow both upward and downward, thus the advancing contact angle is appropriate for use in (4). Breaching pressure for the first intersection of the CHO (Figure 2c) will differ marginally from (4). Experiments in a system approximating the OC geometry [*Wood et al.*, 2002] concluded that minute geometrical imperfections would lead to the formation of two sequential capillary barriers. The first barrier is breached when water pooled above the intersection connects with one of the horizontal fractures. The second barrier forms as shown in Figure 2b. Breaching pressure for this geometry, along with those in Figures 2d and 2e is given by

$$h_{\max} = \frac{\sigma}{\rho_w g b}\left[\cos\alpha + \cos({}^{\pi}/_{4})\right] \quad (5)$$

As suggested by *Glass et al.* [2003], a barrier to the wetting fluid that follows (4) would breach at positive pressure because curvature of the meniscus on the bottom of the pool must reverse direction to bulge into the intersection. Conversely, where $\alpha \leq 45°$, barriers that follow (5) will breach under tension, thus $h_{\max}$ will be smaller than predicted by (4).

2.2. Discharge and Subsequent Reestablishment of Capillary Barriers

[14] The breaching of a capillary barrier causes some of the stored fluid to be discharged. Fluid geometry during discharge cannot be described using the two-dimensional quasi-static approach employed to develop (4) and (5). Instead we provide a mechanistic description of how the discharge process evolves, and leads to either reestablishment of the capillary barrier or development of a fracture spanning fluid tendril. We also show how the capillary barrier can act as a gate to fluid stored in adjoining horizontal fractures.

[15] Where the barrier breaches into an underlying vertical fracture (Figures 2a, 2b, 2d, and 2e), water entry pressure will reinforce gravity and draw water from the pool into the lower fracture through a capillary constriction that spans the intersection. Conversely, air entry pressure at the top of the pool will resist drainage. Because of hysteresis in the entry pressures (air entry < water entry) the resultant of capillary forces will oppose gravity, causing water invasion of the lower fracture to be fundamentally unstable, and proceed as a gravity-driven finger [e.g., *Nicholl et al.*, 1992, 1994].

[16] The pool height will drop during discharge if recharge to the pool is nonexistent, or occurs at a lower rate than flow into the finger. Below the intersection, tension will increase within the finger as it elongates and flow from above decreases (reduced pool height). If the tension becomes high enough, the finger will snap to vacate the intersection and reestablish the capillary barrier. If the finger does not generate sufficient tension to snap the water column, discharge will occur as a continuous tendril, with a pool above the capillary constriction at the intersection [e.g., *Wood et al.*, 2002; *Glass et al.*, 2003; *Ji et al.*, 2004]. In cases where the finger snaps, discharge ends with the pool at a minimum height ($h_{\min}$). The value of $h_{\min}$ will be much harder to predict than $h_{\max}$ because conditions required to terminate discharge are influenced by capillary hysteresis, gravity, inertial forces, viscous forces, and unknown fluid geometry within both the fracture and the intersection.

[17] The volume of water released during discharge (dynamic storage) is a measure of integration by the intersection. Dynamic storage in a vertical fracture above, or feeding into a capillary barrier is given by $bw(h_{\max} - h_{\min})$. For the OC geometry, *Wood et al.* [2002] also observed that one of the two horizontal fractures contributed to integration by accumulating fluid, and that both participated during discharge. Unlike water pooled above the intersection, dynamic storage in the horizontal fractures is not limited by competition between capillary and gravity forces, and may thus be substantial. As a result, a relatively small volume of fluid stored in the vertical fracture can act as a gate for a much larger volume. For the CVO and CHO intersections (Figures 1b and 1c), dynamic storage may include the zone between capillary barriers as well as

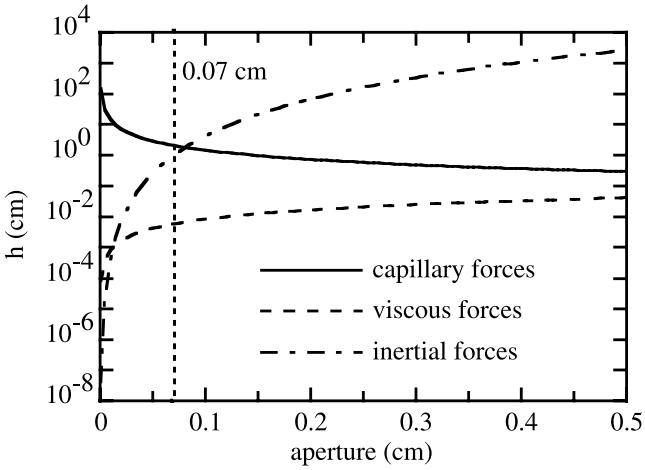

Figure 3. The relative importance of viscous, capillary, and inertial forces shown as a function of aperture (b) in the vertical fracture. Force magnitudes are expressed in terms of hydraulic head (cm) on a logarithmic scale. Assumes pure water at 25°C and perfect wetting of the fracture surfaces ($\alpha = 0°$).

the connected horizontal fractures. Finally, we note that the total volume of water accumulating above and to the sides of an intersection can be substantially greater than the dynamic storage released during integration and will act as a mixing zone.

2.3. Influence of Viscous and Inertial Forces

[18] Fluid velocities may become significant during discharge and thus introduce nonnegligible viscous and/or inertial forces. The magnitude of viscous forces may be expressed in terms of hydraulic head, h_v [L], as

$$h_v = \frac{v\mu}{\rho_w g l} \tag{6}$$

where μ represents kinematic viscosity [M/L-T], v is velocity [L/T], and l is some characteristic length scale [L]. Inertial forces within a moving fluid may be expressed in terms of head, h_i [L], as

$$h_i = \frac{v^2}{2g} \tag{7}$$

As first-order approximations, we assume that v is equivalent to the saturated hydraulic conductivity, K_s, of the fracture [L/T] and that b acts as a characteristic length scale. We can then compare the relative magnitude of viscous and inertial forces to capillary forces as parameterized by the capillary rise (Figure 3). At small b, capillary forces clearly dominate, with inertial forces becoming ascendant at an aperture on the order of 0.08 cm. Viscous forces increase with b, but remain subordinate to either capillary or inertial forces.

[19] Inertial forces may also be a factor when discrete pulses of fluid enter a stagnant pool from above. The transfer of momentum that results when a pulse of volume V_{pulse} moving at a velocity of v, enters a stagnant pool of volume V_{pool} may be expressed as

$$h_i = \frac{v^2}{2g} \bullet \frac{V_{pulse}}{V_{pool}} \tag{8}$$

(8) suggests that transfer of momentum to a pool will be of greatest importance immediately after discharge, when the pool volume is at a minimum.

3. Experimental Design

[20] We created four fracture intersection models that approximated those shown in Figure 1. The models were designed to observe the temporal structure of flow across the intersection as a function of supply rate to the vertical fracture above. On the basis of the mechanistic development in section 2, we set the fracture aperture, b, to ~0.07 cm for all models. This value was chosen to encourage competition between the controlling forces (Figure 3) and to produce a maximum pool height on the order of 1–2 cm; from (5) $h_{\max}$ = 1.5–2 cm for b = 0.07 cm. In this section, we describe construction of the experimental intersections (section 3.1), data acquisition methods (section 3.2), and the experimental sequence (section 3.3).

3.1. Construction of the Experimental Intersections

[21] Three physical models were constructed; one each for the OC, CHO, and CVO geometries (Figures 1a–1c). After completing experiments in the OC model, we modified it to incorporate a CB by inserting a limestone pebble into the intersection (Figure 1d). Each of the three physical models was fabricated using four machined limestone blocks. For the OC and CVO, the four blocks were cut to dimensions of 5.1 × 7.0 × 30.5 cm. In the CVO model, a 1 cm thick spacer was placed at the base of the lower left-hand block to produce a 1 cm vertical offset in the horizontal fracture (Figure 1c). Blocks of two different sizes (5.1 × 7.0 × 30.5 cm and 5.1 × 5.7 × 30.5 cm) were used to create an ~1 cm offset in the vertical fracture for the CHO model (Figure 1b). The 1 cm offsets were chosen to facilitate coupling between the adjacent "T" intersections.

[22] In order to provide a uniformly small contact angle for the surfaces of our analog fractures, we fabricated our models using a water wettable porous media in a near saturated condition. The material used in this investigation is a fine-grained, dolomitic limestone from the Ordovician Oneota formation that was quarried in Le Sueur County, Minnesota. This particular material was chosen for hydraulic properties (porous, low permeability, hydrophilic), durability, uniformity, and ease of machining. Hydraulic tests on representative samples yielded average values for porosity of ~15% and saturated hydraulic conductivity (K_s) of 7 × 10^{-5} cm/min at 21°C [*Wood et al.*, 2004]. We cut the limestone into slightly oversize blocks with a rock saw, and then used a thickness sander to true the faces, square the edges to 90°, remove saw marks, and bring the blocks to dimension. After machining, the blocks were washed thoroughly, saturated under vacuum in chemically equilibrated tap water, and then assembled into the models without contaminating the fracture surfaces.

[23] Each group of four limestone blocks was assembled within a simple enclosure that held the blocks rigidly in

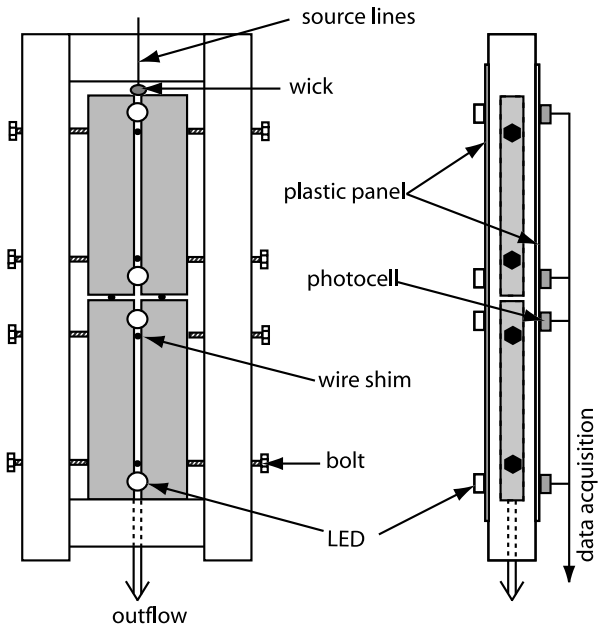

Figure 4. Sketch illustrating the experimental apparatus that holds four limestone blocks within a simple frame of 6.5 × 6.5 cm square tubing. Hex bolts inserted through the tubing hold the blocks in place.

place and restricted evaporation (Figure 4). The frame of the enclosure was fabricated from 6.5 × 6.5 cm square section fiberglass reinforced plastic tubing (1 cm wall thickness). To restrict evaporation, faces of the enclosure were covered with clear plastic panels (0.64 cm thick). The plastic panels allowed an unobstructed view into the fracture planes, including the intersection, and provided mounting points for the sensors (see below). After assembling each model, it was affixed to a rigid test stand and aligned so that the intersecting fractures were true vertical and horizontal.

[24] Fracture apertures were held open by inserting ~0.5 cm long shims cut from 0.08 cm diameter wire. Four shims were placed in each vertical fracture, and three in each horizontal fracture; placements were chosen to minimize interference with flow. The pressure used to hold the blocks in place (see Figure 4), embedded the wire shims slightly, producing apertures of 0.07 cm, as measured by a thickness gauge. This choice of aperture facilitates identification of aperture-spanning flow by our data collection system, falls within the range found for natural fractures [e.g., *Snow*, 1970; *Belfield*, 1994; *Hakami and Larsson*, 1996], and encourages competition between viscous, capillary, and inertial forces (see Figure 3). Assuming flow of pure water at 25°C between parallel plates separated by 0.07 cm, the cubic law [e.g., *Bird et al.*, 1960] leads to an estimate of $K_s = \sim 2.7 \times 10^3$ cm/min for the fractures, much larger than the measured value for the limestone blocks ($\sim 7 \times 10^{-5}$ cm/min). For small α, $b = 0.07$ cm leads to a capillary rise of ~2 cm, and an expected maximum pool height on the order of 1–2 cm.

[25] A positive displacement pump was used to supply chemically equilibrated and filtered (0.2 μm) tap water to a 5 cm long fiberglass wick (0.79 cm diameter) pressed across the top of the vertical fracture (Figure 4). The wick dampened pressure fluctuations from the fluid source, and provided a conduit for water to freely enter the fracture. All other fracture boundaries were left open to atmospheric pressure within the experimental enclosure. Outflow from the bottom of the vertical fracture exited the experiment through a vertical tube. We measured inflow and outflow gravimetrically (0.1 g resolution) at 1-min intervals throughout the experiment to obtain the supply rate and evaporative losses (~0.08 mL/min).

3.2. Characterization of Fracture Flow With Optical Sensors

[26] The temporal structure of flow entering and exiting the intersection was continuously monitored by using purpose-built sensors to measure the transmission of light across the vertical fracture. Output from a light emitting diode (LED) was directed horizontally through the fracture plane onto a photo diode positioned on the opposite side of the fracture at the same elevation (Figure 4). With the fracture empty, light transmission between the LED and photo diode is unimpeded, leading to a high output from the diode. Aperture-spanning water interferes with light transmission through the fracture, thus reducing diode output. This approach allows us to place sensors close to the intersection without impacting flow processes, and to collect data at very high temporal resolution (20 ms intervals). However, to use this approach, the fracture aperture must be large enough to allow clean transmission

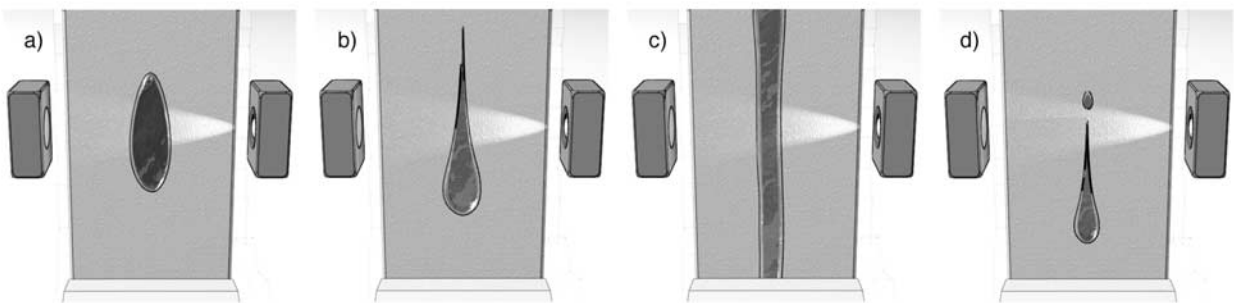

Figure 5. Four general types of flow behavior within the fractures distinguished by our optical sensors: (a) discrete droplets moving downward as an elliptical mass, (b) droplets with a tail, (c) a continuous tendril, and (d) a satellite droplet, which is a very small droplet following a much larger one with a long tail.

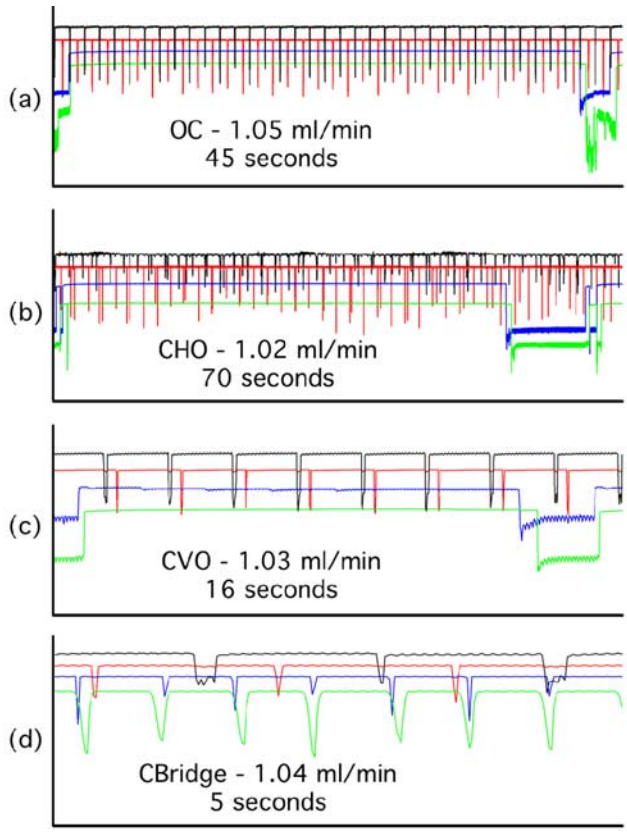

Figure 6. (a–d) Illustrations of signals taken from each model at a supply rate of ~1 mL/min. Duration of each example was chosen to illustrate discharge from the intersection. For each experiment, voltage signals from the optical sensors were evaluated to obtain measures of flow above and below the intersection. Voltage traces represent signals from each sensor: first (top, black), second (red), third (blue), and fourth (bottom, green). A small discrete pulse of fluid (droplet) passing the sensor is recorded as a downward spike. Pulses of longer duration produce an extended downward excursion of the voltage signal that begins with a sharp downward spike, then often tapers off before abruptly returning to the baseline (dry) voltage signal.

of the light beam (~0.04 cm or larger), and small enough so that flow spans the aperture (i.e., contacts both fracture walls). Finally, because the mechanisms for reducing light transmission include refraction, reflection, and absorption, the magnitude of the decrease in diode output is indicative of, but not linearly dependent on the amount of water within the light path.

[27] Two optical sensors were located in the upper vertical fracture (24 cm and 7 cm above the intersection), and two in the lower vertical fracture (4 cm and 23 cm below the intersection). The sensors immediately above and below the intersection were used to characterize the temporal signal of flows entering and exiting the intersection. For that purpose, they were placed as close to the intersection as possible without interfering with visual observations or being obscured by the pooling of fluid above the upper capillary barrier. The uppermost and lowermost sensors provided a level of redundancy and allowed for rough estimates of droplet velocity in the vertical fractures. The intersection itself was left unobstructed to allow visual observation, occasional direct measurement of pool height, and the collection of digital video over selected intervals.

[28] The optical sensors allowed us to discriminate between four general types of flow behavior within the fractures. These include discrete droplets moving downward as an elliptical mass (Figure 5a), droplets with a tail (Figure 5b), a continuous tendril (Figure 5c), and a satellite drop, which is a very small droplet following a much larger one with a long tail (Figure 5d). Example output signals from the optical sensors are shown as Figure 6. A sharp downward spike in the voltage signal indicates that a small discrete pulse of fluid (droplet) passed the sensor (red and black lines in Figures 6a–6c). Larger fluid pulses create an extended downward excursion in the voltage signal that typically begins with a sharp decline in voltage that is followed by a slight increase, and then a sharp return to baseline. This signal (i.e., blue and green lines in Figure 6c) represents a droplet with a large head and narrower tail. The length of the tail increased with supply rate, until finally, the tail reached sufficient length to form a tendril of fluid conducting flow along the fracture plane. Tendrils were identified by a continuous depression of the voltage signal (not shown). *Su et al.* [1999] reported a similar transition from pulsed flow to a stable tendril for gravity-driven unsaturated flow between parallel glass plates with a step increase in aperture. Occasionally, the tail of a pulse would bifurcate, and pass the sensor as a satellite droplet, in which a small pulse follows the larger one (i.e., blue and green lines in Figure 6b); we also observed cases of multiple satellite droplets, where two small pulses would follow the main one.

3.3. Experimental Sequence

[29] Our interest was to explore the range of behavior where the interplay between capillary, gravitational, viscous, and inertial forces would act to impose a temporal signal on flow across the intersection. We performed extensive pretesting to select a representative range of supply rates for the final experiments. At 5 cm of width, saturated flow in the vertical fracture under unit gradient (fracture capacity) would be ~ 940 cm^3/min. At supply rates of ~15 mL/min, we observed a continuous fluid tendril both above and below the intersection in all of our models. We also observed water pooled above the intersection and filling the horizontal fractures, which indicates that the intersections behaved as capillary constrictors. At higher flow rates, multiple tendrils appeared that migrated about the fracture plane both above and below the intersection.

[30] To focus on temporal behavior imposed by the intersection, we considered supply rates between 0.30 and ~15 mL/min. The lower bound was set to exceed evaporative losses (~0.08 mL/min). For each of our four models, we established initial conditions by running chemically equilibrated tap water through the system overnight at ~2 mL/min to assure equilibrium with a satiated matrix. We then started at a supply rate high enough to produce a continuous tendril spanning the system (~15 mL/min), and collected data until at least 200 mL of fluid had passed through the system. Flow was then decreased to a lower rate for another 200 mL, and the process repeated until we

Table 1. Flow Rates for Experimental Steps by Model Type

Step	OC, mL/min	CHO, mL/min	CVO, mL/min	CB, mL/min
1	16	14	16	15
2	7.7	6.8	7.2	7.4
3	5.5	5.9	5.3	5.4
4	3.4	4.1	3.2	4.3
5	2.3	2.3	2.1	2.1
6	1.8	1.7	1.9	1.8
7	1.6	1.5	1.7	1.6
8	1.4	1.4	1.4	1.4
9	1.3	1.2	1.2	na
10	1.1	1.0	1.0	1.0
11	0.88	0.87	0.78	0.85
12	0.68	0.65	0.65	0.68
13	0.48	0.47	0.47	0.50
14	0.33	0.30	0.33	0.31

reached the lowest supply rate of ~0.30 mL/min (Table 1). A volume of 200 mL was chosen to avoid unnecessarily long experiments at low flows but sufficiently large to capture the range of dynamic behavior at higher supply rates.

4. Results

[31] In each experiment, we first established a stable flow regime. Next, we observed and measured the timing of flows within the vertical fracture as the supply rate was stepped down. At the initial supply rate (~15 mL/min), the horizontal fractures were filled and continuous fluid tendrils spanned the vertical fractures from inlet to outlet, with water pooled above a capillary constriction at the intersection. Mass balance considerations place width of the tendrils at ~0.1 cm. Stepping down the supply rate led to complex behavior within the fractures and at the intersection as the tendrils intermittently snapped and reformed. At a supply rate of ~1.5–2 mL/min, flows in all four models became much more regular, both above and below the intersection. Three of the models (OC, CHO, CVO) developed characteristic integration and discharge cycles that became increasingly resistant to change (robust) as supply rate decreased. In these characteristic cycles, pulsed flow entering the intersection from above was accumulated and then released as larger, less frequent pulses below. This temporal integration did not occur in the fourth model. Instead, the CB acted to meter flow across the intersection, releasing fluid as smaller and more rapid drips than those arriving from above. We begin this section by describing the characteristic behaviors observed at low supply rates (section 4.1) and then analyze data streams across all supply rates (section 4.2).

4.1. Characteristic Behaviors at Low Supply Rates

[32] At supply rates of less than ~1.5–2 mL/min, each of our model intersections developed a characteristic behavior in which fluid moved through the vertical fracture in regular pulses, with different temporal signals above and below the intersection (Figure 6). In the CB, small output pulses exited the intersection more frequently than larger pulses arrived from above (Figure 6d). For the other models (OC, CHO, CVO), output pulses were less frequent than the input (Figures 6a–6c). Each of these latter three models displayed a characteristic integration and discharge cycle in which water was temporarily stored in aperture spanning pools within the vertical and sometimes horizontal fractures. The degree of integration within a characteristic cycle is characterized by the discharge volume, which we obtain from the supply rate and interval between discharges. Measurements of minimum (h_{min}) and maximum (h_{max}) pool heights above the intersection were used to calculate dynamic storage in the vertical fracture, while storage in the horizontal fractures was estimated from mass balance. For each intersection we describe the observed behavior, supporting our observations with example data from the optical sensors (Figure 6) and illustrations developed from video taken at selected intervals during each experiment (Figures 7–9).

4.1.1. Orthogonal Cross (OC)

[33] The orthogonal cross displayed a regular integration and discharge cycle at supply rates below ~1.4 mL/min. The optical sensor data (Figure 6a) shows that numerous short-duration pulses entering the intersection (red trace) are

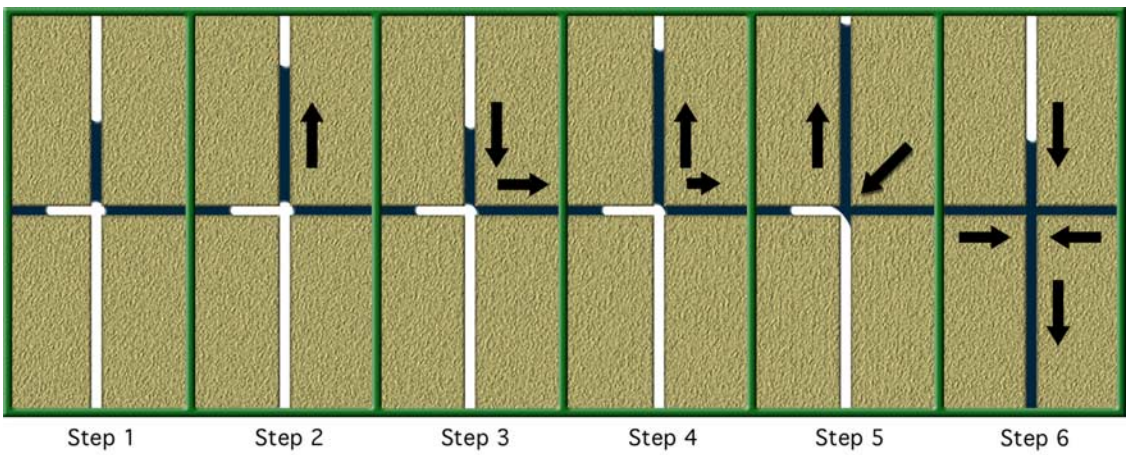

Figure 7. Illustrations of fluid accumulation and discharge in the orthogonal cross intersection over a ~40 s period at a supply rate of ~1 mL/min. Each panel shows a 3.5 cm high by 1.8 cm wide region about the intersection; dark areas within the fractures are occupied by water, while the light areas are empty.

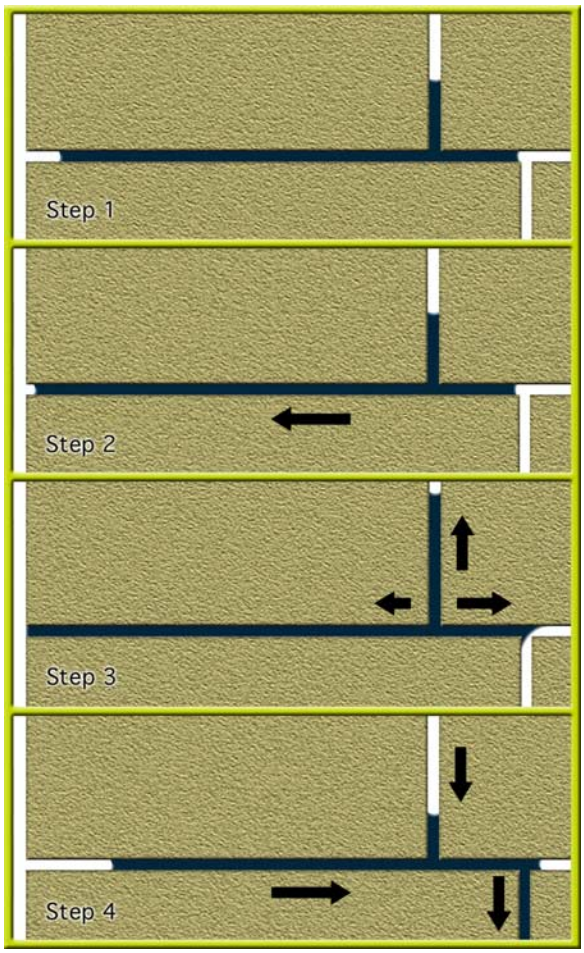

Figure 8. Illustrations of fluid accumulation and discharge in the CHO intersection over a ~44 s period at a supply rate of ~1 mL/min. Each panel shows a 1.9 cm high by 6.0 cm wide region about the intersection; dark areas within the fractures are occupied by water, while the light areas are empty.

accumulated, then released as less frequent, longer duration pulses (blue trace). The OC forms two capillary barriers, and follows a six-step integration and discharge process (below and Figure 7) that was originally reported by *Wood et al.* [2002].

[34] 1. After a discharge event, water is pooled in both horizontal fractures and above the intersection (h_{min} = ~0.5 cm). None of the pools are connected. The pool in the right-hand horizontal fracture abuts the intersection, while the pool in the left-hand fracture is retracted. Neither pool extends fully to the outside edges of the horizontal fracture (not shown).

[35] 2. The upper pool rises with continued addition of water. Increased fluid pressure causes the meniscus along the bottom of the pool to flatten downward until it connects with fluid in the right-hand fracture, breaching the first capillary barrier at h_p = ~1.1 cm.

[36] 3. The upper pool drains into the right-hand fracture more rapidly than new fluid is added from above, lowering h_p to ~0.8 cm.

[37] 4. The upper pool rises as storage in the right-hand fracture fills. Increased fluid pressure causes the meniscus connecting the upper and right-hand fractures to grow downward into the intersection.

[38] 5. The second capillary barrier is breached when the lower meniscus touches the upper corner of the lower left-hand block (illustration shows the meniscus just prior to contact). The pool height required to breach this second capillary barrier (h_p = ~1.3 cm) is greater than for the first barrier (step 2).

[39] 6. Water fills the intersection and enters the left-hand horizontal fracture to connect with the existing pool and fill the remaining storage. The lower vertical fracture is invaded as a gravity-driven finger. The pool above the intersection decreases to a minimum as water flows out of storage in the upper and both horizontal fractures. The finger thins to a tendril as it advances (tension increases due to the action of the hanging column within the finger), eventually "snapping" to vacate the intersection and produce a condition similar, but not necessarily identical to that at the beginning of the process (step 1). The cycle is then repeated.

[40] The OC formed two capillary barriers in each cycle, both of which breached under tension. The first barrier breached when the pool above the intersection connects with the pool in the right-hand horizontal fracture (h_{max} ~1.1 cm). The second barrier breached when the coalesced pool contacts the upper corner of the lower left-hand block (h_{max} ~1.3 cm). Total discharge per event was ~0.90 mL, with ~0.22 mL released from storage in the upper pool. The remaining ~0.68 mL of discharge is partitioned between dynamic storage in the horizontal fractures and resupply during discharge.

4.1.2. Cross With Horizontal Offset (CHO)

[41] The cross with horizontal offset displayed a regular integration and discharge cycle at supply rates below ~1.7 mL/min. The optical sensor data (Figure 6b) shows discharge pulses (blue) that narrow behind the leading edge to form an extended tail. The four-step integration and discharge sequence for the single capillary barrier formed at this intersection is shown in Figure 8 and described as follows.

[42] 1. After a discharge event, a single pool fills most of the left-hand horizontal fracture (pool is retracted toward the intersection by ~0.4 cm) and extends into the upper fracture (h_{min} ~0.5 cm).

[43] 2. Additional fluid goes into storage within the left-hand horizontal fracture, which grows toward the left-hand edge of the model (away from the intersection).

[44] 3. As storage in the left-hand horizontal fracture fills, the pool begins to grow upward into the vertical fracture. The resulting increase in h_p causes the meniscus on the right-hand side of the pool to flatten and grow into the intersection. The capillary barrier is breached at h_{max} = ~0.9 cm, when the meniscus contacts the upper corner of the lower right-hand block (illustration shows the meniscus just prior to contact).

[45] 4. Water fills the intersection, invading the lower vertical fracture as a gravity-driven finger. A small tongue of water lashes out into the right-hand fracture a distance of about 0.3 cm. During discharge, the finger thins to a tendril, height of the upper pool declines, and the pool in the left-hand horizontal fracture retracts to ~0.6–1 cm from the left-hand edge of the fracture. When the tendril snaps to vacate the intersection, the pool in the left-hand fracture

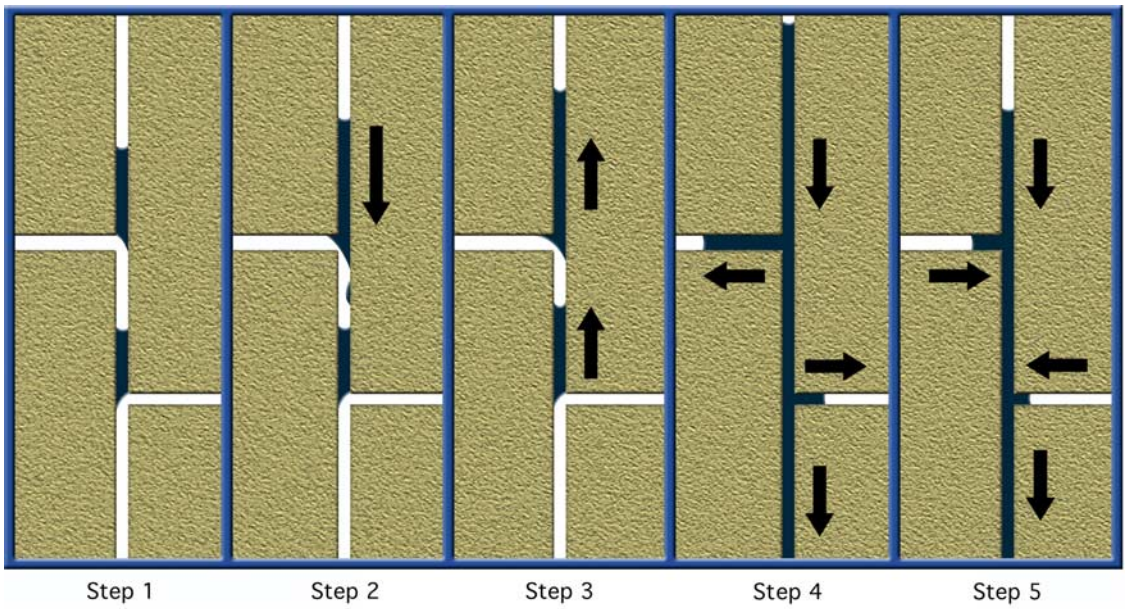

Figure 9. Illustrations of fluid accumulation and discharge in the CVO intersection that occurred over a ~7 s period at a supply rate of ~1 mL/min. Each panel shows a 2.9 cm high by 1.3 cm wide region about the intersection; dark areas within the fractures are occupied by water, while the light areas are empty.

springs back to within ~0.4 cm from the far edge. Normally, the right-hand fracture is emptied when the tendril snaps, but occasionally a small (~0.2–0.4 cm diameter) fluid blob is left behind. The cycle is then repeated.

[46] The CHO had the potential for two capillary barriers, one at each of the "T" intersections. The first (inverted "T") did not drain as flow was stepped down, leaving the second (normal "T") as the sole capillary barrier. Total discharge per event was ~0.87 mL, with ~0.14 mL from storage in the vertical fracture. The remaining ~0.73 mL of discharge is partitioned between dynamic storage in the horizontal fracture and resupply during discharge. With respect to the OC intersection, the capillary barrier formed in the CHO is somewhat weaker (smaller h_{min}) but acts as a gate to a slightly larger storage volume in the horizontal fracture.

4.1.3. Cross With Vertical Offset (CVO)

[47] The cross with vertical offset settled into a regular integration and discharge cycle at supply rates below ~3.2 mL/min. Representative optical sensor data (Figure 6c) shows limited integration, and discharge events of short duration. The vertical offset between the upper and lower sideways "T" intersections found in this geometry led to the formation of two separate capillary barriers along the vertical fracture. Interaction between the two barriers and lack of storage in the horizontal fractures combined to produce a less robust integration and discharge cycle than for the OC or CHO. The most commonly observed sequence is shown in Figure 9 and described as follows.

[48] 1. After a discharge event, both horizontal fractures are empty, and the vertical fracture contains two pools. One pool is directly above the upper horizontal fracture (upper pool, h_{min} = ~0.5 cm) and the other is above the lower horizontal fracture (lower pool, h_{min} = ~0.3 cm).

[49] 2. A pulse of water enters the upper pool from above. In response, the lower meniscus of the pool flexes downward into the intersection and releases a small packet of fluid to the lower pool, which traveled as a gravity-driven film finger along one side of the fracture. Thus both pools grow, with the upper pool growing faster.

[50] 3. The meniscus on the bottom of the upper pool advances into the intersection with increasing h_p. Discharge of the upper pool occurs at $h_p \sim 1.0$ cm, when flexure of the bottom meniscus from drop impact induces contact with the corner of the lower left-hand brick (illustration shows the meniscus just prior to contact).

[51] 4. The upper and lower pools connect and discharge as one. A tongue of water lashes ~0.3 cm into the upper horizontal fracture, while a smaller tongue of water invades the lower horizontal fracture. A gravity-driven finger moves downward in the vertical fracture below the lower intersection.

[52] 5. As height of the combined pools declines, the finger thins to a tendril and the tongues of water are retracted from the horizontal fractures. The upper intersection vacates first, then the lower intersection vacates to conclude discharge. The cycle is then repeated.

[53] The sequence described above was sensitive to minor perturbations. An interesting variant occurred when the tongue of water that invades the upper horizontal fracture during step 4 occasionally snapped off and was left behind. The presence of this small amount of water (0.3–0.4 cm wide) abutting the vertical fracture greatly increased the volume of fluid transferred from the upper pool to the lower pool in step 2 (above). Visually, it appeared as if the pulse passed through the upper pool to strike the lower pool. The perturbation of the drop striking the lower pool caused a deflection in the bottom meniscus that released a small packet of fluid, which travels as a film finger along the left side of the lower vertical fracture (this is very similar to step 2 described above). As the pool height of the lower pool increases, the lower meniscus moves

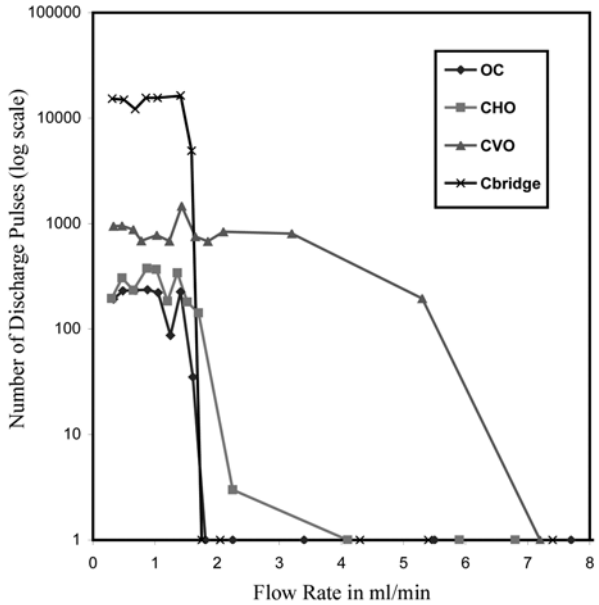

Figure 10. The number of discharge pulses per 200 mL of flow as a function of fluid supply rate. A continuous tendril is considered to be a single pulse.

further into the lower intersection. Failure of the lower barrier appeared to occur simultaneously with contact of the meniscus with the lower right hand brick and connection of the upper meniscus of the lower pool with the trapped blob in the left horizontal fracture. Note that the vertical separation between the two intersections was ~1.0 cm, which coincides with h_{max} for the upper intersection.

[54] This model also differed from the others in that inertial forces had a substantial influence on behavior. Impact of water droplets on the upper surface of a pool led to flexure of the bottom meniscus. Depending on circumstances, flexure of the meniscus could release a small packet of fluid, or induce discharge. Packets of fluid released by flexure would travel as an unstable film (gravity-driven film finger) seen as a film "bump" along one side of the fracture (e.g., Figure 9, step 2). Film flow from the upper pool would be trapped at the lower pool, while packets released from the lower pool would exit the intersection. The size of the fluid packet visibly decreased as pool volume increased. This inverse relation between inertial effects and pool volume is consistent with (8), which suggests that increased mass in a pool will attenuate the momentum of the pulse hitting it, thereby reducing the deflection of the lower surface. With respect to the CVO intersection, pools formed by both the CHO and the 2nd barrier of the OC geometries involve greater storage volumes, making them less susceptible to inertial effects. The 1st capillary barrier of the OC intersection is less susceptible to inertial effects than the CVO geometry because the meniscus is pinned on both sides of the fracture, rather than being free to slide along one of the facture surfaces.

[55] Integration capacity of the CVO intersection was limited to the vertical fracture. Total discharge per event was ~0.24 mL, with ~0.18 mL released from storage in the upper pool. The remaining ~0.06 mL of discharge is partitioned between storage in the lower pool and resupply during discharge.

4.1.4. Capillary Bridge

[56] A limestone pebble (~0.1 cm in diameter) was inserted ~2.5 cm into the intersection of the OC in a manner that assured point contacts were made with the corners of the limestone blocks. Doing so created a local capillary bridge (i.e., a continuous water film) across the intersection. This eliminated the integration and discharge cycle seen in the other models. Instead, the CB showed a different type of regular behavior at supply rates below ~1.6 mL/min. Water pooled above the intersection (h_p ~ 0.8 cm) was metered out into the fracture below in small, more frequent pulses. Optical sensor data (Figure 6d) clearly shows fewer pulses entering the intersection (red) than exiting (blue). The upper pool remains in a quasi-steady state that balances pulsed drain to the lower fracture with pulsed resupply from above. The left-hand horizontal fracture remained dry except adjacent to the intersection, while the right-hand fracture stayed fully filled. Fluid storage in the horizontal fractures did not appear to fluctuate during discharge. Our observations suggest that flow across the intersection is constricted as flow thins across the limestone pebble.

[57] Below the intersection, pulsation occurs as a gravity-driven finger repeatedly forms and then detaches from the capillary constriction to move independently downward as a droplet. This is a standard mechanism for the initiation of gravity-driven fingers from steady supply to a point source [e.g., *Nicholl et al.*, 1993a]. Fluid enters the fracture from the capillary constriction and grows downward as a hanging column. When the length of the hanging column places sufficient tension to cause detachment, the droplet breaks free and advances downward. Given the fracture aperture (~0.07 cm), relatively little tension is required for detachment, which leads to small droplets.

4.2. Optical Sensor Data

[58] Optical sensors were employed to characterize the temporal behavior of flow along the vertical fractures. The influence of the intersection is most closely measured at sensor 3, which is located directly below to capture discharge behavior (see example placement in Figure 4). For each model, we characterized behavior at Sensor 3 over a time interval that spanned 200 mL of supply volume. Data at the highest flow rates showed the presence of a continuous fluid tendril in all models (i.e., no signal was imposed by the intersection). However, in each model, the intersection imposed a temporal signal (pulsed flow) as the supply rate was stepped down. For pulsed flow regimes, we measured the number of pulses during each 200 mL flow step and the interval between successive pulses. The latter was defined as the elapsed time between the start of a given pulse and the start of the next one (see Figure 5).

[59] As a gross measure of system behavior, we first present the total number of fluid pulses discharged during each 200 mL flow step (Figure 10). At high supply rates, flow occurred as a continuous fluid tendril from inlet to outlet, which we treat as a single discharge pulse. At low supply rates, each model settled into a regular integrate and discharge cycle as described in section 4.1. Between these

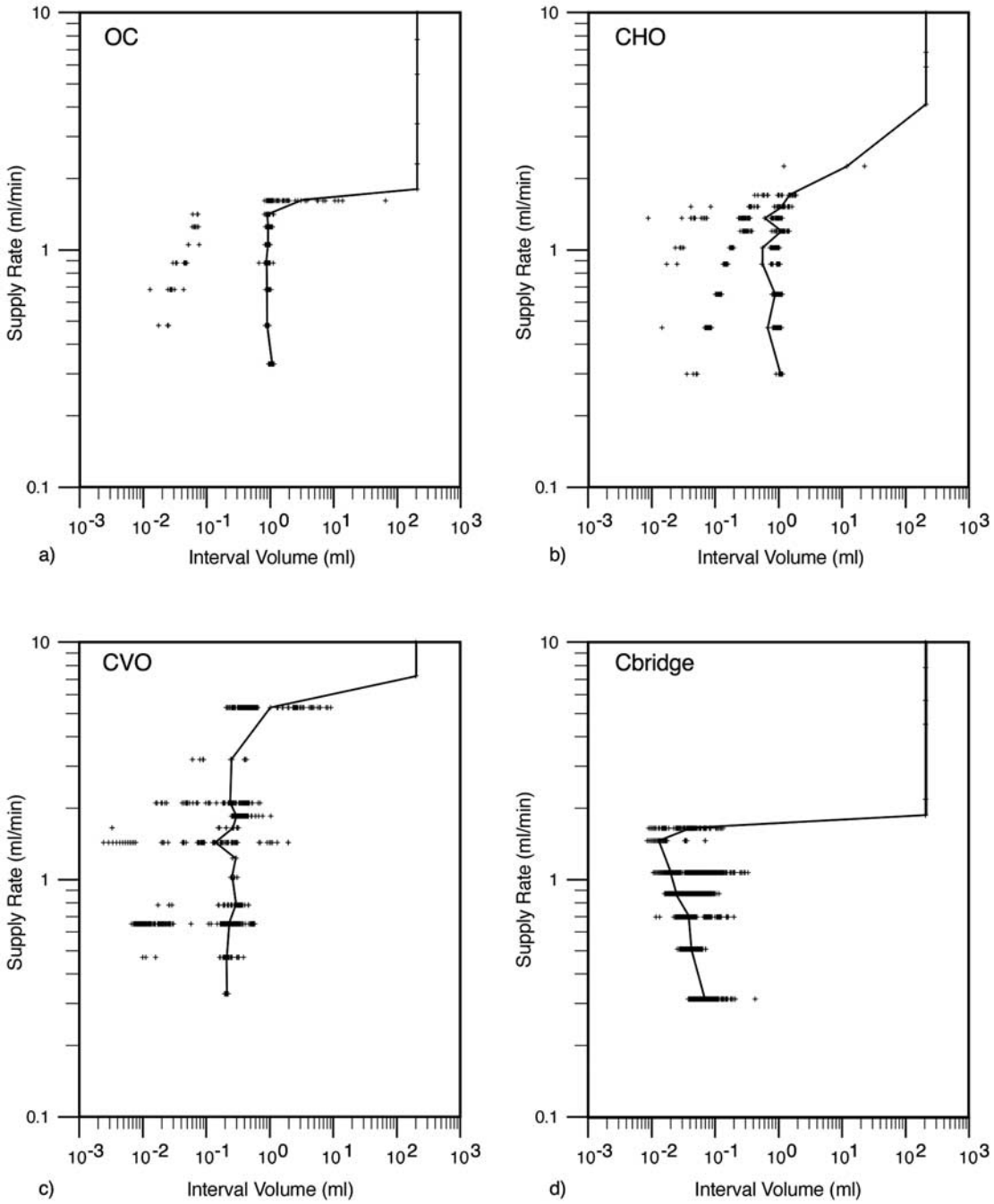

Figure 11. Interval volume (in mL) at sensor 3 as a function of supply rate: (a) OC, (b) CHO, (c) CVO, and (d) capillary bridge (labeled Cbridge). Solid line follows the mean interval volume at each supply rate.

two regimes was a transition zone where continuous tendrils snapped and reformed. Analogous transitions between dripping and jetting are reported in the literature addressing the classic dripping faucet problem [e.g., *Ambravaneswaran et al.*, 2004]. The transition zone was widest for the CVO, where flow experienced complicated interactions between the two separate capillary barriers at each sideways "T" intersection. The CB demonstrated the sharpest transition from a continuous tendril to individual drops, suggesting an abrupt change in fluid detachment behavior as flow across the limestone bridge drops below a threshold capable of supporting a stable tendril. At low supply rates the OC and CHO displayed the fewest number of pulses (∼200), reflecting the relatively high degree of integration in those models that rises from the addition of dynamic storage in the horizontal fractures to that present in the vertical fracture. Dynamic storage within the horizontal fractures was negligible in the CVO intersection, leading to reduced integration and a higher number of pulses (∼1000). The most pulses were observed for the CB (∼15,000), which did not integrate flow, but instead metered it out as high-frequency pulses.

Table 2. Summary of Statistical Measures Calculated From Interval Volume Data Listed by Model Geometry Versus the Average of Flow Rates for Experimental Test Step

Average q, mL/min	OC Interval				CHO Interval				CVO Interval				CB Interval			
	Mean, mL	SD	Kurtosis	Skew	Mean, mL	SD	Kurtosis	Skew	Mean, mL	SD	Kurtosis	Skew	Mean, mL	SD	Kurtosis	Skew
15	200	na	na	na	200	na	na	na	200	na	na	na	200	na	na	na
7.3	200	na	na	na	200	na	na	na	200	na	na	na	200	na	na	na
5.5	200	na	na	na	200	na	na	na	1.0	1.5	9.8	3.0	200	na	na	na
3.8	200	na	na	na	200	na	na	na	0.25	0.017	97	−0.81	200	na	na	na
2.2	200	na	na	na	11	14	na	na	0.24	0.051	23	1.7	200	na	na	na
1.8	200	na	na	na	1.4	0.24	7.5	−2.6	0.30	0.051	86	7.6	200	na	na	na
1.6	3	8	53	7.0	1.1	0.37	0.17	−1.2	0.27	0.018	74	−4.8	0.04	0.01	5	2
1.4	0.89	0.13	33	−5.6	0.59	0.35	−1.8	0.023	0.14	0.12	88	6.8	0.01	0.002	−1	1
1.3	0.90	0.17	20	−4.5	1.1	0.32	1.4	−1.4	0.29	0.001	430	−18	na	na	4	2
1.0	0.90	0.10	59	−7.5	0.54	0.37	−1.9	0.003	0.26	0.014	−0.80	0.94	0.02	0.01	1	2
0.85	0.85	0.19	14	−3.8	0.53	0.39	−2.0	0.027	0.29	0.042	9.2	−1.9	0.02	0.01	1	1
0.67	0.86	0.21	11	−3.6	0.86	0.30	2.2	−1.9	0.23	0.11	0.91	−0.33	0.04	0.01	−1	1
0.48	0.87	0.12	47	−6.7	0.66	0.39	−1.3	−0.8	0.21	0.020	39	−1.2	0.04	0.004	20	4
0.32	1.0	0.05	−1.4	−0.06	1.0	0.19	23	−4.9	0.21	0.005	0.73	−0.83	0.07	0.01	6	2

[60] In pulsed flow regimes that involve integration of flow (OC, CHO, CVO), the interval between successive discharge pulses will be dependent on supply rate; i.e., dynamic storage will fill more slowly at low supply rates, leading to a longer interval between discharge events. To remove this flow rate dependency, we multiplied each pulse interval by the appropriate supply rate to obtain the interval volume, I_v, (L^3). This quantity describes the amount of fluid entering the system during a given pulse, and serves as a surrogate for discharge volume, which cannot be measured directly in our design. Data for I_v are shown in Figure 11 and the statistical measures are presented in Table 2; in both, continuous tendrils are represented by I_v = 200 mL. The mean values of I_v are plotted on Figure 11 as solid lines. Note also that many of the individual data points on Figure 11 are coincident.

[61] The three integrative models (OC, CHO, CVO) show behaviors that are similar to one another (Figure 11), and very different from the flow metering model (CB). As flow is stepped down, each of the integrative models passes through a transition zone where continuous tendrils snap and reform before the model settles into its characteristic low-flow behavior (see also Figure 10). The snapping tendrils occurring within the transition zones exhibit a wide range of durations, leading to a high standard deviation (σ) for I_v (Table 2). Despite the relatively high value of σ, each of the integrative models exhibits a positive kurtosis within the transition zone, suggesting a distribution more peaked than would be expected for normally distributed data. The distributions of I_v are also skewed, with the OC and CVO showing a skew toward larger values and the CHO toward smaller. Note however that a relatively small number of discharge events occur within the transition zones.

[62] At lower supply rates (∼1–2 mL/min), the integrative models settle into the characteristic behaviors described in section 4.1. The emergence of a regular cycle removes most of the dependency of I_v on supply rate and greatly reduces the standard deviation of I_v with respect to that observed in the transition zone. The standard deviation would be further reduced except for the presence of satellite drops in the discharge signal. These small pulses follow a larger event (Figure 5d) and reflect the bifurcation of the thin liquid thread connecting the primary drop to the fluid remaining in the intersection. The occurrence of paired primary and satellite droplets has long been known to occur when fluid drips from a capillary tube into the open air [*Edgerton et al.*, 1937]. Continued interest in the topic of satellite droplets [e.g., *Notz et al.*, 2001; *Ambravaneswaran et al.*, 2002] has been driven by engineering applications (e.g., jetting).

[63] In our experiments, the occurrence of the short-duration satellite events tends to increase σ and skews the distribution of I_v toward small values; i.e., the skew of I_v is negative or near zero at most of the low-flow rates (Table 2). For the OC (Figure 11a), the mean value of I_v is uniformly near 0.90 mL and independent of supply rate at flows of 1.4 mL/min and below. At low supply rates, the CHO (Figure 11b) also shows a relatively constant mean value of I_v (∼0.87 mL). Satellite drops were frequent, and of longer duration than for the OC, leading to higher values of σ. For the CVO, the mean value of I_v was relatively constant (∼0.24 mL) over a large range of flow rates; however, the

data show more scatter and less uniform satellite drops. The maximum interval volume was nearly an order of magnitude smaller than for the OC and OHC. The small storage volume, susceptibility to inertial forces, and coupling between the two capillary barriers in the CVO all contributed to creating less uniform and smaller interval volumes.

[64] Behavior of the CB intersection (Figure 11d) differs significantly from that observed for the integrative models (OC, CHO, CVO). The transition from a stable tendril to individual drops is much sharper than in the integrative models, and I_v does not remain constant after the model settles into its characteristic behavior. The lowest mean interval volume ($\sim$ 0.13 mL) occurs at a supply rate of 1.4 mL/min, mean I_v then increases to $\sim$0.67 mL as the supply rate declines. The literature on dripping from a capillary tube into the open atmosphere suggests the opposite, that drop volume will decrease with supply rate [*Zhang and Basaran*, 1995]. The difference in our system is that the droplet forms within a water-wettable fracture rather than in the open atmosphere. In both cases, drop detachment will be controlled by drop length and air-water geometry at the detachment point. In our experiment, film thickness around the capillary bridge is expected to increase with supply rate. This should lead to amore robust connection and thus not be responsible for the observed behavior. Conversely, low-flow rates are expected to produce less elongate droplets that will grow to larger volume than the more elongate droplets formed at high supply rates.

5. Discussion

[65] In our experiments, flow in the vertical fractures was dominated by gravity-driven fingers. In general, fluid entering from the source or discharging from the intersection formed fingers that narrowed behind the finger tip with depth under increased tension. At high supply rates, fingers developed into stable fracture spanning tendrils [e.g., *Glass et al.*, 2003; *Ji et al.*, 2004]. At very low supply rates, small symmetric droplets traversed the fracture. Film flow along the vertical fractures [e.g., *Tokunaga and Wan*, 1997] was only observed to occur in the CVO model where it played a limited role in transferring fluid between the upper and lower pools.

[66] Except for the CB, discharge from all of our model fracture intersections was controlled by a single local geometry. This principal capillary barrier is formed by a meniscus that connects perpendicular flat surfaces (i.e., vertical and horizontal) as shown in Figure 2b, 2d, and 2e. The meniscus is free to slide along both surfaces, and the barrier is breached when the meniscus comes into contact with the opposite corner of the lower block (e.g., step 5 in Figure 7 and step 3 in Figures 8 and 9). Because the meniscus is not pinned, this barrier geometry fails under tension, rather than the positive pressure expected for the symmetric behavior depicted in Figure 2a. The behavior depicted by Figure 2a is highly sensitive to small perturbations, and unlikely to occur in any real system. Further, the first failure of such a symmetric meniscus would lead to pooling in one of the horizontal fractures, which then induces a preferential direction for future behavior.

[67] Assuming $\alpha = 0°$, (5) predicts $h_{max} = 1.8$ cm. Our measurements were of similar order. We measured maximum pool height above the intersection at $\sim$1.3 cm for the OC, $\sim$0.9 cm for the CHO, and $\sim$1.0 cm for the CVO. In each case, the pool also invaded downward, so those values must be increased by 0.07–0.1 cm to obtain an estimate of h_{max}. Equation (5) is not highly sensitive to α, predicting $h_{max} = 1.5$ cm at $\alpha = 45°$. Likewise, small errors in estimating b cannot fully account for the observed discrepancy. More likely explanations for the overestimation of h_{max} by (5) are geometric imperfections, deformation of the unsupported bottom meniscus under gravity, and/or inertial effects. The capillary barrier breaches on contact with the opposite corner of the model. Any local protrusion of that corner into the intersection would lead to breaching at a lower value of h_{max} than is predicted by (5). Also, derivation of (5) assumes a symmetric interface. However, the lowest portion of the interface will be subject to slightly higher pressure than the upper portion and may deform accordingly. Because the interface is both relatively large and not pinned in place, small pressure differences may lead to substantial deformation. Finally, we observed clear evidence of inertial effects in the CVO model, where drop impact on the pool initiated breaching. Inertial effects may have had a more subtle influence on breaching in the other models.

[68] Dynamic storage in the vertical fracture places a lower limit on the degree of integration by an intersection, which may be significantly augmented by dynamic storage in the horizontal fracture(s). The OC requires that a horizontal fracture be involved in the breaching process, as does the CHO. In both cases, storage in the horizontal fracture(s) exceeded that in the vertical fracture. For the CVO, invasion of the horizontal fractures during discharge occurs under the tension applied by a gravity-driven finger, which curtails advancement [see also *Glass et al.*, 2003]. As the tension increases, the water that moved into the horizontal fracture retracts and the fracture is vacated. The participation of horizontal fractures complicates predicting the degree of integration. Over many preliminary experiments, we found pools within the horizontal fracture to range from persistent to ephemeral to nonexistent, with a corresponding range of integration. Slight variations in fracture aperture and orientation of the intersection in the gravitational field can result in large differences in storage volume. Finally, in our experiments, storage capacity was limited by the outside edge of the bricks. One can easily imagine larger storage volumes in natural systems.

[69] The presence of a capillary bridge removed the temporal integration behavior and forced an essentially static pool along the path of a gravity-driven finger. Analogous behavior has been observed within fractures, where aperture variability can impose a localized pool and drip structure along a gravity-driven finger [e.g., *Nicholl et al.*, 1993a; *Glass and Nicholl*, 1996; *Su et al.*, 1999]. The capillary bridge (limestone pebble in our model) provides a capillary connection that acts to restrict flow across the intersection. At a given supply rate, pool height above the constriction and conductivity of the connecting geometry come into equilibrium.

[70] At the lowest supply rates, pulsed flow arriving at the OC, CHO, and CVO intersections slowly accumulates in dynamic storage, and is then rapidly discharged. Because of the difference in timescales between the two processes,

integration is effectively decoupled from discharge, and behavior is stable. At higher supply rates, fluid is added to dynamic storage during discharge events, coupling the two processes. Increased coupling between integration and discharge coincides with erratic behavior characterized by intermittent tendrils that are sensitive to minor perturbations. At the highest supply rates, tendrils are stabilized by viscous forces, and extend from inlet to outlet. The capillary constriction formed at the intersection leads to pooling of water in the vertical fracture above the intersection, and in the horizontal fractures. All models, including the CB passed through flow regimes where behavior was erratic. Although we did not see direct evidence of chaotic behavior, the possibility is suggested by the obvious analogies between our system and the dripping faucet problem, which is known to exhibit chaotic regimes [*Shaw*, 1984].

[71] Although our work here focused on temporal behavior, we can easily infer how our simplistic intersections would influence the spatial characteristics of network-scale flow. For the OC geometry, vertical flow will initially invade only one side of the horizontal fracture. In a network of such intersections, neighboring vertical fractures are likely to connect through a horizontal pool, which then discharges through the single intersection with the lowest breaching pressure. This integration mechanism was identified in the experiments of *LaViolette et al.* [2003] and *Wood et al.* [2004]. In networks of CVO intersections, pressure required to enter a vertical fracture from a horizontal fracture will exceed the breaching pressures for barriers along the throughgoing vertical fractures. Thus the intersections act to ''maintain'' narrow vertical pathways, which leads to the formation of a ''slender ladder'' structure with depth [*Glass et al.*, 2003]. Our experiments suggest that when the CVO is offset by more than the maximum pool height, water may never reach the adjoining intersection of the abutting horizontal fracture, thus emphasizing the slender ladder behavior even more strongly.

[72] A network of CHO intersections is expected to integrate multiple pathways and maintain narrow pathways. Consider two vertical fractures abutting a horizontal fracture, each with a horizontal offset. For flow down both of the vertical fractures, the intersection between the two will be invaded from both sides, which facilitates breaching [e.g., *Glass and Yarrington*, 1996] and thus integration of the two pathways. Meanwhile, the outer intersections act as barriers that maintain the converged pathway. CB intersections likely do not behave as strongly as OC, CVO, or CHO intersections as pathway integrators and/or maintainers. However, as a minimum, the pool above a CB (or for that matter, any of the other intersections) has the potential to integrate multiple pathways within an individual fracture, and form a single pathway entering the lower vertical fracture. In fact, it was this minimal behavior that *Glass et al.* [1995] suggested could lead to large-scale confluencing of flow within a fracture network.

6. Concluding Remarks

[73] The mechanisms involved in the rapid percolation of water along focused pathways in the deep vadose zone are not fully understood. Gravity-driven fingers within individual fractures are likely to play an important role; however, network influences, particularly the capillary heterogeneity imposed by fracture intersections has received little attention. In earlier work [*Wood et al.*, 2002], we found that a simple intersection between orthogonal fractures, one horizontal and the other vertical, could act to integrate unsaturated flows. At low flows the intersection formed a capillary barrier that accumulated flow from above, then released the integrated volume as a pulse below. To further understand this behavior, we evaluated the mechanisms that lead to capillary barrier formation and breeching at intersections between horizontal and vertical fractures. Using that information for design, we repeated our previous experiment, and considered three perturbations to that simple orthogonal cross, including one that was designed to circumvent the capillary barrier. In each case, we found that low steady flow was impacted by the intersection. Gravity-driven fingers within the fractures were captured by the intersections, then released into the fracture below with an altered signal (temporal and magnitude).

[74] Three of the intersection geometries (OC, CHO, CVO) developed a regular integration and discharge cycle, while the fourth, which was designed to circumvent integration, acted to meter flow into the fracture below. Despite differences in geometry, each of the three integrative models formed a single penultimate capillary barrier, in which the meniscus of a pool slides along two perpendicular fracture surfaces and fails under tension. At the lowest flows considered, each of these intersections conformed to well defined integration and discharge behavior. Breaching and reestablishment of the capillary barrier was controlled by pool height in the vertical fracture above the intersection, which was similar between the geometries. However, differences in participation by the horizontal fractures led to substantial variation in the degree of integration. As supply rate increased, behavior entered a transition zone where it was erratic, with intermittent fluid tendrils forming both above and below the intersections. At higher supply rates we observed a steady regime where continuous tendrils spanned both vertical fractures. The tendrils were connected by a capillary constriction across the intersection that caused water to pool above and fill both horizontal fractures. The fourth model (CB), behaved as a capillary constrictor at all flow rates. At low supply rates, restricted flow through the constriction led to rapid pulsation in the lower facture where a gravity-driven finger repeatedly formed and snapped.

[75] Results suggest two regimes for low steady flow in unsaturated fractured networks with a transition between. At the lowest flows, pulsation along individual pathways is suggested, while at somewhat higher flows, results suggest steady flow controlled by capillary constrictions. For either regime (pulsating or constrictor controlled), we should expect the flow structure within the fractured vadose zone to be composed of distributed pools above and/or to either side of intersections that are connected by gravity-driven fingers. Given the behavior of intersections to maintain and integrate pathways [e.g., *Glass et al.*, 2003; *LaViolette et al.*, 2003], we should also expect that large-scale flow structure will tend toward global convergence with depth. A competing mechanism not interrogated in our experiments is the action of fracture intersections to split flow, or to switch between outlet fractures; both of which would work against large-scale convergence, and may occur in both the

pulsating and the constrictor regimes. The effect of outlet switching has been considered numerically by *Glass and LaViolette* [2004]. Their results suggest that the presence of intersections that switch between outlets will work against large-scale convergence of flow and contribute toward the formation of a self-organized state characterized by fluid avalanches across a wide range of scales. The same authors also used numerical means to explore the potential effects of flow path splitting in response to convergence [*LaViolette and Glass*, 2004]. Overloading of intersections along pathways was found to lead to splitting and the activation of new pathways.

[76] **Acknowledgments.** We thank Fred White and Tim McJunkin for technical support and data processing. We are grateful for the support from the Environmental Systems Research Program under contract number DE-AC07-99ID13727 from the Office of Environmental Management, Department of Energy, to the Idaho National Engineering and Environmental Laboratory. Data analysis and the writing of this manuscript were supported by the U.S. Department of Energy's Environmental Management Science Program under contract DE-AC07-99ID13727 at the Idaho National Engineering and Environmental Laboratory, DE-FG07-02ER63499 at the University of Idaho, and DE-AC04-94AL85000 at Sandia National Laboratories.

References

Ambravaneswaran, B., E. D. Wilkes, and O. A. Basaran (2002), Drop formation from a capillary tube: Comparison of one-dimensional and two-dimensional analyses and occurrence of satellite drops, *Phys. Fluids*, *14*(8), 2606–2621.

Ambravaneswaran, B., H. J. Subramani, S. D. Phillips, and O. A. Basaran (2004), Dripping-jetting transitions in a dripping faucet, *Phys. Rev. Lett.*, *93*(3), 034501, doi:10.1103/PhysRevLett.93.034501.

Belfield, W. C. (1994), Multifractal characteristics of natural fracture apertures, *Geophys. Res. Lett.*, *21*(24), 2641–2644.

Bird, R. B., W. E. Stewart, and E. N. Lightfoot (1960), *Transport Phenomena*, 780 pp., John Wiley, Hoboken, N. J.

Dahan, O., R. Nativ, M. Adar, B. Berkowitz, and Z. Ronen (1999), Field observation of flow in a fracture intersecting unsaturated chalk, *Water Resour. Res.*, *35*(11), 3315–3326.

Davidson, G. R., R. L. Bassett, E. L. Hardin, and D. L. Thompson (1998), Geochemical evidence preferential flow of water through fractures in unsaturated tuff, Apache Leap, *Appl. Geochem.*, *13*, 184–195.

Dragila, M. I., and N. Weisbrod (2004), Fluid motion through an unsaturated fracture junction, *Water Resour. Res.*, *40*, W02403, doi:10.1029/2003WR002588.

Edgerton, H. E., E. A. Hauser, and W. B. Tucker (1937), Studies in drop formation as revealed by the high-speed motion camera, *J. Phys. Chem.*, *41*, 1017–1027.

Fabryka-Martin, J. T., P. R. Dixon, S. S. Levy, B. Liu, D. L. Brenner, L. E. Wolfsberg, H. J. Turin, and P. Sharma (1996), Implications of environmental isotopes for flow and transport in the unsaturated zone at Yucca Mountain, Nevada, *Geol. Soc. Am. Abstr. Programs*, *28*(7), A-416.

Faybishenko, B. A., R. Salve, P. Zawislanski, K. H. Lee, P. Cook, B. Freifeld, K. Williams, and C. Doughty (1998), Ponded infiltration test at the Box Canyon site: Data report and preliminary analysis, *Rep. LBNL-40183*, Lawrence Berkeley Natl. Lab., Berkeley, Calif.

Faybishenko, B., C. Doughty, S. Steiger, J. Long, T. Wood, J. Jacobsen, J. Lore, and P. Zawislanski (2000), Conceptual model of the geometry and physics of water flow in a fractured basalt vadose zone, *Water Resour. Res.*, *36*(12), 3499–3520.

Glass, R. J., and R. A. LaViolette (2004), Self organized spatial-temporal structure within the fractured vadose zone: Influence of fracture intersections, *Geophys. Res. Lett.*, *31*, L15501, doi:10.1029/2004GL019511.

Glass, R. J., and M. J. Nicholl (1996), Physics of gravity-driven fingering of immiscible fluids within porous media: An overview of current understanding and selected complicating factors, *Geoderma*, *70*, 133–163.

Glass, R. J., and V. C. Tidwell (1991), Research program to develop and validate conceptual models for flow and transport through unsaturated fractured rock, in *Proceedings of the Second Annual International Conference on High Level Radioactive Waste Management*, pp. 977–987, Am. Nucl. Soc., Las Vegas, Nev.

Glass, R. J., and L. Yarrington (1996), Simulation of gravity fingering in porous media using a modified invasion percolation model, *Geoderma*, *70*, 231–252.

Glass, R. J., M. J. Nicholl, and V. C. Tidwell (1995), Challenging models for flow in unsaturated, fractured rock through exploration of small scale flow processes, *Geophys. Res. Lett.*, *22*(11), 1457–1460.

Glass, R. J., M. J. Nicholl, and V. C. Tidwell (1996), Challenging models for flow in unsaturated, fractured rock through exploration of small scale processes, Sandia National Laboratories, Albuquerque, NM, SAND95-1824, 61 pp.

Glass, R. J., M. J. Nicholl, A. L. Ramirez, and W. D. Daily (2002a), Liquid phase structure within an unsaturated fracture network beneath a surface infiltration event: Field experiment, *Water Resour. Res.*, *38*(10), 1199, doi:10.1029/2000WR000167.

Glass, R. J., M. J. Nicholl, S. E. Pringle, and T. R. Wood (2002b), Unsaturated flow through a fracture-matrix network: Dynamic preferential pathways in mesoscale laboratory experiments, *Water Resour. Res.*, *38*(12), 1281, doi:10.1029/2001WR001002.

Glass, R. J., M. J. Nicholl, H. Rajaram, and T. R. Wood (2003), Unsaturated flow through fracture networks: Evolution of liquid phase structure, dynamics, and the critical importance of fracture intersections, *Water Resour. Res.*, *39*(12), 1352, doi:10.1029/2003WR002015.

Hakami, E., and E. Larsson (1996), Aperture measurements and flow experiments on a single natural fracture, *Int. J. Rock Mech. Min. Sci. Geomech. Abstr.*, *33*(4), 395–404.

Ji, S.-H., M. J. Nicholl, R. J. Glass, and K.-K. Lee (2004), Influence of a simple fracture intersection on density-driven immiscible flow: Wetting vs. nonwetting flows, *Geophys. Res. Lett.*, *31*, L14501, doi:10.1029/2004GL020045.

LaViolette, R. A., and R. J. Glass (2004), Self organized spatio-temporal structure within the fractured vadose zone: The influence of dynamic overloading at fracture intersections, *Geophys. Res. Lett.*, *31*, L18501, doi:10.1029/2004GL020659.

LaViolette, R. A., R. J. Glass, T. R. Wood, T. R. McJunkin, K. S. Noah, R. K. Podgorney, R. C. Starr, and D. L. Stoner (2003), Convergent flow observed in a laboratory-scale unsaturated fractured system, *Geophys. Res. Lett.*, *30*(2), 1083, doi:10.1029/2002GL015775.

Nativ, R., E. Adar, O. Dahan, and M. Geyh (1995), Water recharge and solute transport through the vadose zone of fractured chalk under desert conditions, *Water Resour. Res.*, *31*(2), 253–261.

Nicholl, M. J., and R. J. Glass (2002), Field investigation of flow processes associated with infiltration into an initially dry fracture network at Fran Ridge, Yucca Mountain, Nevada: A photo essay and data summary, *Rep. SAND2002-1369*, 75 pp., Sandia Natl. Lab., Albuquerque, N. M.

Nicholl, M. J., R. J. Glass, and H. A. Nguyen (1992), Gravity-driven fingering in unsaturated fractures, in *Proceedings of the Third Annual International Conference on High Level Radioactive Waste Management*, pp. 321–331, Am. Nucl. Soc., Las Vegas, Nev.

Nicholl, M. J., R. J. Glass, and H. A. Nguyen (1993a), Small-scale behavior of single gravity-driven fingers in an initially dry fracture, in *Proceedings of the Fourth Annual International Conference on High Level Radioactive Waste Management*, pp. 2023–2032, Am. Nucl. Soc., Las Vegas, Nevada.

Nicholl, M. J., R. J. Glass, and H. A. Nguyen (1993b), Wetting front instability in an initially wet unsaturated fracture, *Proceedings of the Annual International Conference on High Level Radioactive Waste Management*, pp. 2061–2070, Am. Nucl. Soc., Las Vegas, Nev.

Nicholl, M. J., R. J. Glass, and S. W. Wheatcraft (1994), Gravity-driven infiltration flow instability in non-horizontal unsaturated fractures, *Water Resour. Res.*, *30*(9), 2533–2546.

Notz, P. K., A. U. Chen, and O. A. Basaran (2001), Satellite drops: Unexpected dynamics and change of scaling during pinch-off, *Phys. Fluids*, *13*(3), 549–552.

Podgorney, R. K., T. R. Wood, B. A. Faybishenko, and T. M. Stoops (2000), Spatial and temporal instabilities in water flow through variably saturated fractured basalt on a one-meter field scale, in *Dynamics of Fluids in Fractured Rocks*, *Geophys. Monogr. Ser.*, vol. 122, edited by B. Faybishenko, P. A. Witherspoon, and S. M. Benson, pp. 129–146, AGU, Washington, D. C.

Russell, C. E., J. W. Hess, and S. W. Tyler (1987), Hydrogeologic investigation of flow in fractured tuffs, Rainier Mesa, Nevada Test Site, in *Flow and Transport Through Unsaturated Fractured Rock*, *Geophys. Monogr. Ser.*, vol. 42, edited by D. D. Evans and T. J. Nicholson, pp. 43–50, AGU, Washington, D. C.

Shaw, R. (1984), *The Dripping Faucet as a Model Chaotic System*, Aerial, Santa Cruz, Calif.

Snow, D. T. (1970), The frequency and apertures of fractures in rock, *Int. J. Rock Mech. Min. Sci.*, *7*, 23–40.

Su, G. W., J. T. Geller, K. Pruess, and F. Wen (1999), Experimental studies of water seepage and intermittent flow in unsaturated, rough-walled fractures, *Water Resour. Res.*, *35*(4), 1019–1037.

Tokunaga, T. K., and J. Wan (1997), Water film flow along fracture surfaces of porous rock, *Water Resour. Res.*, *33*(6), 1287–1295.

Wood, T. R., M. J. Nicholl, and R. J. Glass (2002), Fracture intersections as integrators for unsaturated flow, *Geophys. Res. Lett.*, *29*(24), 2191, doi:10.1029/2002GL015551.

Wood, T. R., R. J. Glass, T. R. McJunkin, R. K. Podgorney, R. A. LaViolette, K. S. Noah, D. L. Stoner, R. C. Starr, and K. Baker (2004), Unsaturated flow through a small fracture-matrix network: part 1. Experimental observations, *Vadose Zone J.*, *3*, 90–100.

Yang, I. C., G. W. Rattray, and P. Yu (1996), Interpretation of chemical and isotopic data from boreholes in the unsaturated zone at Yucca Mountain, Nevada, *U.S. Geol. Surv. Water Resour. Invest. Rep., 96-4058*, 58 pp.

Zhang, X., and O. A. Basaran (1995), An experimental study of dynamics of drop formation, *Phys. Fluids*, *7*(6), 1184–1203.

R. J. Glass, Flow Visualization and Processes Laboratory, Sandia National Laboratories, Albuquerque, NM 87185, USA. (rjglass@sandia.gov)

M. J. Nicholl, Geoscience Department, University of Nevada, Las Vegas, NV 89154, USA. (michael.nicholl@ccmail.nevada.edu)

T. R. Wood, Idaho National Engineering and Environmental Laboratory, Idaho Falls, ID 83415, USA. (tqw@inel.gov)